

High-efficient machine learning projection method for incompressible Navier-Stokes equations

Ruilin Chen^{1,2}, Xiaowei Jin¹, Nikolaus A. Adams³, and Hui Li^{1,4,*}

¹School of Civil Engineering, Harbin Institute of Technology, Harbin 150090, China

²College of Shipbuilding Engineering, Harbin Engineering University, Harbin 150001, China

³School of Engineering and Design, Technical University of M nch, M nch 85748, Germany

⁴Faculty of Computing, Harbin Institute of Technology, 150001, China

* Author to whom correspondence should be addressed: lihui@hit.edu.cn

Abstract. Hybrid simulation that integrating traditional numerical methods with artificial intelligence offers great potential for enhancing computational efficiency in fluid dynamics. High-fidelity data is one of most critical issues for the successful applications of AI in fluid mechanics, which is expensively obtained or even inaccessible. This study proposes a high-efficient machine learning (ML) projection method using forward-generated data for incompressible Navier-Stokes equations. A Poisson neural network (Poisson-NN) embedded method and a wavelet transform convolutional neural network multigrid (WTCNN-MG) method are proposed, integrated into the projection method framework in patchwork and overall differentiable manners with MG method, respectively. The solution of the pressure Poisson equation split from the Navier-Stokes equations is first generated either following a random field (e.g. Gaussian random field, GRF, computational complexity $\mathcal{O}(N \log N)$, N is the number of spatial points) or physical laws (e.g. a kind of spectra, computational complexity $\mathcal{O}(N \cdot M)$, M is the number of modes), then the source terms, boundary conditions and initial conditions are constructed via balance of equations, avoiding the difficulties of obtaining high-fidelity training datasets. The feasibility of generated data for training Poisson-NN and WTCNN as well as the acceleration performances of the Poisson-NN embedded method and WTCNN-MG method are validated. The results indicate that even without any DNS data, the generated data can train these two models with excellent generalization and accuracy. The data following physical laws can significantly improve the high-frequency approximation, convergence rate, generalization and accuracy than that generated following GRF. The ML projection method offers significant improvements in computational efficiency. Particularly, the Poisson-NN embedded method achieves an average speed-up of 5.83 times over the traditional MG method, while the WTCNN-MG method offers an even greater average speed-up of 7.03 times, demonstrating impressive acceleration performance.

Keywords: Hybrid simulation, machine learning projection method, data forward generation, incompressible Navier-Stokes equations, Poisson equation

1. Introduction

Artificial intelligence (AI) has become a powerful tool in fluid mechanics [1, 2], which can help in finding new phenomenon or physical laws (classification function) [3], and modeling (regression function) [4]. Integrating machine learning (ML) techniques with traditional numerical methods represents a promising direction in computational fluid mechanics (CFD). Traditional methods ensure accuracy and stability for most problems, while ML models excel at rapidly approximating physical models, offering new approaches to improve solver performance.

One of examples in the hybrid paradigm is that ML accelerates CFD, such as ML has been employed to estimate spatial derivatives on low-resolution grids [5], calibrate low-resolution numerical solutions [6], embed into traditional numerical frameworks to partially replace computationally expensive steps

[7], etc. Furthermore, ML models are integrated with solvers such as Jacobi [8] and conjugate gradient (CG) [9] methods or used to design better preconditioners for CG [10], achieving faster solution speeds while maintaining accuracy. These hybrid methods are mainly combined in a patchwork manner, and the ML models are purely data-driven, which often limits their applicability and generalizability.

Machine learning has also provided innovative approaches to optimize the performance of multigrid (MG) method, a powerful solver that typically relies on expert-defined parameters and operations. ML-driven approaches, such as using stochastic gradient descent (SGD) to optimize restriction and prolongation matrices [11, 12], constructing mapping from discrete matrices to prolongation operators [13, 14], and employing reinforcement learning to drive graph coarsening strategies [15], significantly improve the convergence performance of MG. Notably, He and Xu [16] first revealed the close connection between MG and convolutional neural network (CNN), demonstrating that pooling, transposed convolution and feature extraction in CNN directly correspond to restriction, prolongation and iterative smoothing in MG, respectively, and proposed MgNet, providing an opportunity for combining CNN and MG. Chen et al. [17] further introduced a new hypernetwork into MgNet based on meta-learning, which generates smoothers tailored for MgNet. Meanwhile, Fanaskov [18] proposed a matrix-free neural multigrid (NMG) structure that uses convolutional operations for equivalent computations, with network training analogous to finding optimal smoothing points. These ML models primarily focus on optimizing the restriction and prolongation matrices of MG to enhance spectral properties and convergence, essentially using ridge regression. Furthermore, these models still rely on the existing MG framework, which is constrained by its theoretical limits, necessitating new improvement mechanisms.

Despite significant advances in AI for fluid mechanics, a major challenge remains its reliance on massive amount of high-fidelity flow field datasets for training. Currently, there is a consensus on the importance of continuously accumulating direct numerical simulations (DNS) or high-resolution experimental data, as emphasized in [2], which encourages the academic community to further establish comprehensive open-source databases. However, the computational or experimental costs of such high-fidelity datasets are extremely high, time-consuming, and frequently unattainable in many practical applications, making data acquisition an expensive prerequisite.

A high-efficient machine learning projection method using forward-generated high-fidelity data for solving incompressible Navier-Stokes equations is proposed in this study. ML models are embedded in the projection method framework to efficiently solve the most computationally expensive pressure Poisson equation (PPE), and massive amount of high-fidelity data is high-efficiently forward-generated satisfying the governing partial differential equations (PDEs) of fluids, which make the ML models training be available. The feasibility of this method is validated in the Poisson neural network (Poisson-NN) embedded method and a wavelet transform convolutional neural network multigrid (WTCNN-MG) method for accelerating the solution of the incompressible Navier-Stokes equations.

The rest of this paper is structured as follows. Section 2 first introduces the basic framework of the ML projection method and two embedding ideas in patchwork and overall differentiable manners, and then introduces the GRF-based and spectra-constraint-based generation methods for high-fidelity flow field solutions and data pairs satisfying governing PDEs. Section 3 verifies the feasibility of generated

data for training Poisson-NN and WTCNN as well as the acceleration performances of the Poisson-NN embedded method and WTCNN-MG method. Section 4 draws the conclusions.

2. Methodology

2.1. ML projection method for incompressible Navier-Stokes equations

The projection method is widely used for solving incompressible Navier-Stokes equations. The second-order explicit-implicit time discrete form, Adams-Bashforth for convection and Crank-Nicolson for viscosity, is written as follows [19],

$$\frac{\mathbf{u}^* - \mathbf{u}^n}{dt} + \frac{3(\mathbf{u}^n \cdot \nabla) \mathbf{u}^n - (\mathbf{u}^{n-1} \cdot \nabla) \mathbf{u}^{n-1}}{2} = \frac{1}{Re} \frac{\nabla^2 \mathbf{u}^* + \nabla^2 \mathbf{u}^n}{2} + \mathbf{f}^{n+1}, \quad (1a)$$

$$\nabla^2 \mathbf{p}^{n+1} = \frac{\nabla \cdot \mathbf{u}^*}{dt}, \quad (1b)$$

$$\mathbf{u}^{n+1} = \mathbf{u}^* - dt \nabla \mathbf{p}^{n+1}, \quad (1c)$$

where the superscript n denotes the time step, dt is the time step size, Re is the Reynolds number, and \mathbf{f} represents the external force or source term. To get the flow velocity \mathbf{u}^{n+1} , it is needed to solve pressure Poisson equation (Eq. (1b), PPE) via an intermediate velocity \mathbf{u}^* , which is the most computationally expensive step in the entire numerical process. With appropriate spatial discretization, the algebraic equation of PPE is

$$\mathbf{A} \mathbf{p} = \mathbf{b}, \quad (2)$$

where $\mathbf{A} \in \mathbb{R}^{N \times N}$ is the discrete coefficient matrix, $\mathbf{p} \in \mathbb{R}^N$ is the pressure solution vector, and $\mathbf{b} \in \mathbb{R}^N$ is the right-hand side vector containing boundary conditions.

The traditional iterative method for solving Eq. (2) is expressed as,

$$\mathbf{p}^{(k+1)} = \mathbf{p}^{(k)} + \mathbf{M}^{-1}(\mathbf{b} - \mathbf{A} \mathbf{p}^{(k)}), \quad (3)$$

where superscript k is the iteration index, \mathbf{M}^{-1} is the smoothing or preconditioning matrix. The iteration error $\mathbf{e}^{(k)} = \mathbf{p}^{(k)} - \mathbf{p}$ at the k^{th} iteration satisfies [20],

$$\|\mathbf{e}^{(k)}\|_A \leq 2 \left(\frac{\sqrt{\kappa} - 1}{\sqrt{\kappa} + 1} \right)^k \|\mathbf{e}^{(0)}\|_A, \quad (4)$$

where $\|\mathbf{e}^{(k)}\|_A = \sqrt{\mathbf{e}^{(k)T} \mathbf{A} \mathbf{e}^{(k)}}$, κ is the spectral condition number of $\mathbf{M}^{-1} \mathbf{A}$. The convergence is limited by the initial guess error $\mathbf{e}^{(0)}$ and the spectral condition number of $\mathbf{M}^{-1} \mathbf{A}$, i.e., a good initial guess and a suitable preconditioner (smoother) and are the keys to speeding up the iteration process.

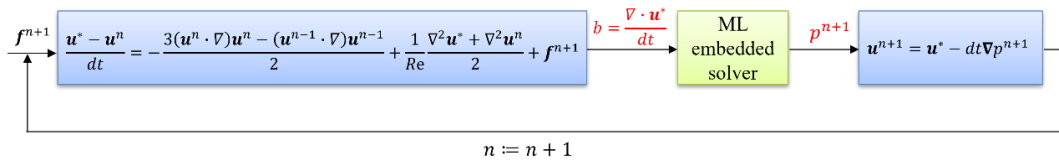


Fig.1. The ML projection method numerical solution framework of incompressible Navier-Stokes equations.

Solving PPE using traditional iterative methods is expensively cost. Therefore, a ML model can be established to approximate the solution of Eq. (1b), further embedded into entire numerical simulation framework as shown in Fig.1 to accelerate the computation of Navier-Stokes equations. A necessary condition for embedding the ML model into the numerical solution framework is that its approximated

solution must meet the required accuracy. Notably, the ML projection method is not limited to the explicit-implicit temporal discretization scheme, but is also applicable to other temporal discretization schemes, as the projection operations (Eq. (1b)) are consistent, and the ML-embedded solver focuses solely on solving Eq. (1b).

Here, two types of ML embedded solvers integrating ML with multigrid solver are proposed: the Poisson-NN embedded solver and the wavelet transform convolutional neural network multigrid (WTCNN-MG) solver. The first adopts patchwork manners, providing a better initial approximation for the MG solver (or directly replacing it if accuracy requirements are met). The second adopts overall differentiable integration manners, breaking the performance bottlenecks of the MG solver

(1) Poisson-NN embedded solver

The Poisson-NN embedded in the numerical solution framework of the incompressible Navier-Stokes equations is designed to serve not merely as a data-driven pressure function approximator but as a physically interpretable PPE solver. The architecture of Poisson-NN is inspired by the analytical solution of the Poisson equation $\nabla^2 p(\mathbf{x}) = b(\mathbf{x})$ expressed using Green's function $G(\mathbf{x}, \boldsymbol{\xi})$ as $p(\mathbf{x}) = \int_{\Omega} G(\mathbf{x}, \boldsymbol{\xi}) b(\mathbf{x}) d\boldsymbol{\xi} + \int_{\partial\Omega} \frac{\partial G(\mathbf{x}, \boldsymbol{\xi})}{\partial n_{\boldsymbol{\xi}}} g(\mathbf{x}) ds_{\boldsymbol{\xi}}$, $\mathbf{x}, \boldsymbol{\xi} \in \Omega$, where $g(\mathbf{x})$ is the boundary function. Two Fourier neural networks $\mathcal{N}_G(\mathbf{x}; \boldsymbol{\theta}_G)$ and $\mathcal{N}_h(\mathbf{x}; \boldsymbol{\theta}_h)$ are employed to approximate the terms in two integrals above, respectively, and the FFT is applied to eliminate the numerical integration using the convolution theorem,

$$p_{NN}(\mathbf{x}) = \mathcal{F}^{-1}\{\mathcal{F}\{\mathcal{N}_G(\mathbf{x}; \boldsymbol{\theta}_G)\}\mathcal{F}\{b(\mathbf{x})\}\} + \mathcal{N}_h(\mathbf{x}; \boldsymbol{\theta}_h). \quad (5)$$

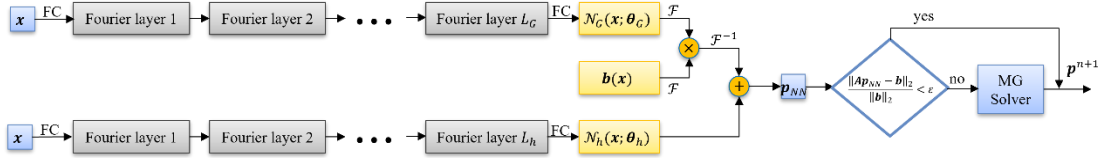


Fig.2. Poisson-NN framework.

The Poisson-NN framework is illustrated in Fig. 2. The subnetworks $\mathcal{N}_G(\mathbf{x}; \boldsymbol{\theta}_G)$ and $\mathcal{N}_h(\mathbf{x}; \boldsymbol{\theta}_h)$ have basically the same structure. Both take the spatial coordinate \mathbf{x} as input, followed by a fully connected (FC) layer, then a stack of L Fourier layers, and finally a FC layer that outputs $\mathcal{N}_G(\mathbf{x}; \boldsymbol{\theta}_G)$ and $\mathcal{N}_h(\mathbf{x}; \boldsymbol{\theta}_h)$, respectively. The operation of the Fourier layer is defined as,

$$h^{l+1}(\mathbf{x}) = \sigma\left(W^l h^l(\mathbf{x}) + \mathcal{F}^{-1}\left\{R^l \mathcal{F}\{h^l(\mathbf{x})\}\right\}\right), \quad (6)$$

where $h^l(\mathbf{x})$ is the feature of the l^{th} hidden layer, W^l and R^l are the trainable parameters of the l^{th} hidden layer, $\sigma(\cdot)$ represents the nonlinear activation function. The right-hand side term of the PPE, $b(\mathbf{x})$, is directly involved in the Fourier transform operation. The accuracy of the pressure field p_{NN} output by Poisson-NN is evaluated. If it meets the preset accuracy requirement ($\frac{\|Ap_{NN} - b\|_2}{\|b\|_2} < \epsilon$), it is directly used for velocity correction (Eq. (1c)). Otherwise, it serves as the initial approximation for the MG solver. This ensures the Poisson-NN embedded numerical solution framework accelerates computation while maintaining accuracy and stability.

The loss function used to guide Poisson-NN optimization training is,

$$\mathcal{L} = \mathcal{L}_p + \mathcal{L}_{eq} + \lambda_\theta \mathcal{L}_\theta = \frac{1}{B} \sum_{i=1}^B \frac{\|p_{NN}^{(i)} - p^{(i)}\|_2^2}{\|p^{(i)}\|_2^2} + \frac{1}{B} \sum_{i=1}^B \frac{\|A_p p_{NN}^{(i)} - b^{(i)}\|_2^2}{\|b^{(i)}\|_2^2} + \lambda_\theta \|\theta\|_2^2, \quad (7)$$

where \mathcal{L}_p , \mathcal{L}_{eq} , and \mathcal{L}_θ represent the supervised pressure matching loss, unsupervised PPE residual loss, and weight decay regularization with coefficient λ_θ , respectively, $\theta = \{\theta_G, \theta_h\}$, $\|\cdot\|_2$ is the Euclidean norm, and B is the mini-batch size. A two-stage training strategy is employed: first in single precision to quickly converge to relatively optimal network parameters, then switched to double precision to meet high-precision requirements.

(2) Wavelet transform CNN multigrid solver

MG numerical simulation is a powerful solver for large-scale PPE (Eq. (2)). We propose a wavelet transform convolutional neural network multigrid (WTCNN-MG) numerical simulation, which not only optimizes the smoothing, differentiation, restriction, and prolongation operations but also integrates WTCNN to perform additional low-frequency error correction on coarse grid levels, fully utilizing ML both advantages in optimization and low-frequency approximation [21].

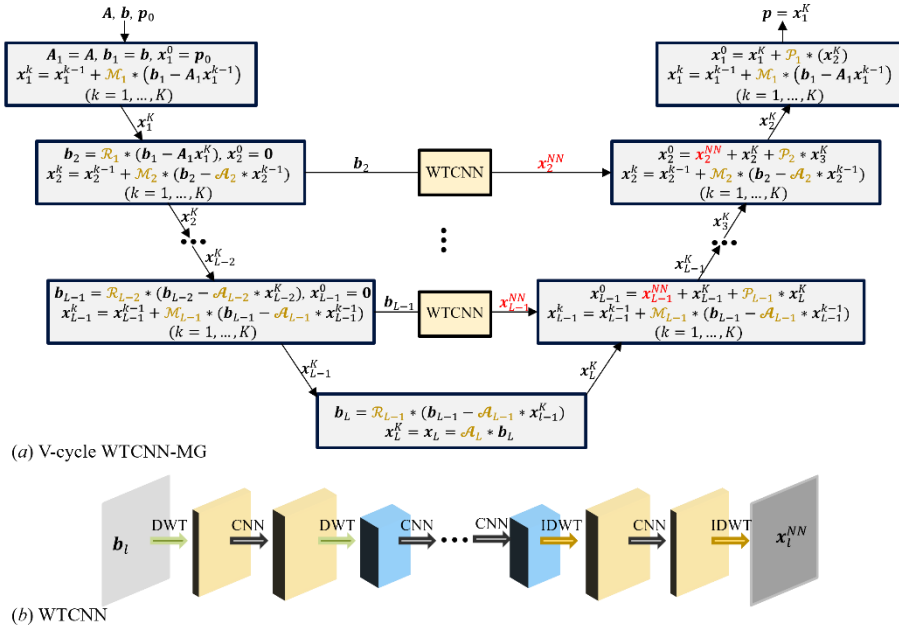


Fig. 3. WTCNN-MG framework, (a) V-cycle WTCNN-MG, (b) WTCNN.

The schematic of a V-cycle WTCNN-MG is illustrated in Fig. 3, with the corresponding algorithm provided in Algorithm 1. At each fine grid level l , the smoothing convolution kernel \mathcal{M}_l ($l = 1, 2, \dots, L-1$) and differentiation convolution kernel \mathcal{A}_l ($l = 2, 3, \dots, L-1$) are used to replace traditional iterative matrix and differential operations in multigrid numerical simulation, respectively. The restriction operation is performed using the restriction convolution kernel \mathcal{R}_l ($l = 1, 2, \dots, L-1$) with a stride of $s > 1$. At the coarsest grid level L , the inverse operation is approximated by the convolution kernel \mathcal{A}_L . The prolongation operation is performed using the prolongation convolution kernel \mathcal{P}_l ($l = 1, 2, \dots, L-1$), which is a transposed convolution operation with a stride of $s > 1$, combined with WTCNN that map right-hand side term b_l to low-frequency smoothing error correction x_l^{NN} ,

$$\mathbf{x}_l^{NN} = \mathcal{W}^{-1}\{\sigma(\mathcal{K} * \mathcal{W}^{-1}\{\sigma(\dots \sigma(\mathcal{K} * \mathcal{W}\{\sigma(\mathcal{K} * \mathcal{W}\{\mathbf{b}_l\})\})\})\})\}, \quad l = 2, \dots, L-1, \quad (8)$$

$$\mathbf{x}_l^0 = \mathbf{x}_l^{NN} + \mathbf{x}_l^K + \mathcal{P}_l * \mathbf{x}_{l+1}^K, \quad l = 2, \dots, L-1, \quad (9)$$

where \mathcal{W} and \mathcal{W}^{-1} represent the discrete wavelet transform (DWT) and its inverse (IDWT), respectively, \mathcal{K} represent the convolution kernel of CNN, $*$ represent the convolution operator.

Algorithm 1: V-cycle WTCNN-MG for $\mathbf{Ap} = \mathbf{b}$

Input: discrete matrix \mathbf{A} , right-hand side \mathbf{b} , initial guess \mathbf{p}_0 , maximum grid level L , smoothing iterations K ;

Output: $\mathbf{p} = \mathbf{x}_1^K$;

Initialization: $\mathbf{A}_1 = \mathbf{A}$, $\mathbf{b}_1 = \mathbf{b}$, $\mathbf{x}_1^0 = \mathbf{p}_0$;

for $l = 1$ to $L-1$ **do**

Pre-smoothing:

for $k = 1$ to K **do**

$$\mathbf{x}_l^k = \mathbf{x}_l^{k-1} + \mathcal{M}_l * (\mathbf{b}_l - \mathcal{A}_l * \mathbf{x}_l^{k-1}), \text{ where } \mathcal{A}_1 * \mathbf{x}_1^{k-1} = \mathbf{A}_1 \mathbf{x}_1^{k-1};$$

end for

$$\text{Restriction: } \mathbf{b}_{l+1} = \mathcal{R}_l * (\mathbf{b}_l - \mathcal{A}_l * \mathbf{x}_l^K);$$

Initial guess: $\mathbf{x}_{l+1}^0 = 0$;

end for

Coarsest grid convolution (approximating inverse): $\mathbf{x}_L^K = \mathcal{A}_L * \mathbf{b}_L$;

for $l = L-1$ to 1 **do**

WTCNN correction: $\mathbf{x}_l^{NN} = \mathcal{W}^{-1}\{\sigma(\mathcal{K} * \mathcal{W}^{-1}\{\sigma(\dots \sigma(\mathcal{K} * \mathcal{W}\{\sigma(\mathcal{K} * \mathcal{W}\{\mathbf{b}_l\})\})\})\})\}$, where $\mathbf{x}_1^{NN} = 0$;

Prolongation: $\mathbf{x}_l^0 = \mathbf{x}_l^{NN} + \mathbf{x}_l^K + \mathcal{P}_l * \mathbf{x}_{l+1}^K$;

Post-smoothing:

for $k = 1$ to K **do**

$$\mathbf{x}_l^k = \mathbf{x}_l^{k-1} + \mathcal{M}_l * (\mathbf{b}_l - \mathcal{A}_l * \mathbf{x}_l^{k-1}), \text{ where } \mathcal{A}_1 * \mathbf{x}_1^{k-1} = \mathbf{A}_1 \mathbf{x}_1^{k-1};$$

end for

end for

Like traditional MG solver, the WTCNN-MG solver consists of multiple V-cycles sequentially connected until the specified convergence condition is met ($\frac{\|\mathbf{Ap}_{NN} - \mathbf{b}\|_2}{\|\mathbf{b}\|_2} < \varepsilon$). Except for the first V-cycle, which receives the given initial guess, all subsequent V-cycles use the output of the previous cycle as their initial guess. Sharing trainable parameters across cycles makes it function as recurrent neural network (RNN), but unlike conventional RNNs trained over the entire sequence, WTCNN-MG is trained independently for each V-cycle. The training loss consists of the unsupervised PPE residual loss and weight decay regularization (\mathcal{L}_{eq} and \mathcal{L}_θ of Eq. (7)). A two-stage training strategy is employed, starting with single precision and transitioning to double precision.

2.2. Method of data forward generation with governing partial differential equations

Conventional way for obtaining training data for ML models involve solving Eq. (1), while our way of thinking is to forward generate flow field solution, then the source terms, boundary conditions and initial conditions are obtained via governing equations, forming data pairs including source terms, boundary conditions, initial conditions and corresponding flow field solutions. The data can be generated either following a random distribution or physical laws. Here, two methods for data forward generation are presented.

(1) Forward generation method of flow field solution with Gaussian random fields

A Gaussian random field (GRF) is defined as a field where samples in any finite set follow a multivariate Gaussian distribution,

$$u(\mathbf{x}) \sim \mathcal{N}(\mu(\mathbf{x}), C(\mathbf{x}, \mathbf{x}')), \quad (10)$$

where $u(\mathbf{x})$ is the samples, $\mu(\mathbf{x})$ is the mean function, $C(\mathbf{x}, \mathbf{x}')$ is the covariance (kernel) function. By selecting appropriate mean and covariance functions, GRFs can produce flow field solutions with certain statistical properties. Typically, the mean function is set to zero, assuming no prior knowledge of the baseline value of the flow field. Considering the flow turbulence, the Matern kernel is adopted as follows,

$$C(\mathbf{x}, \mathbf{x}') = \sigma^2 \frac{2^{1-\nu}}{\Gamma(\nu)} \left(\sqrt{2\nu} \frac{\|\mathbf{x}-\mathbf{x}'\|_2}{\lambda} \right)^\nu K_\nu \left(\sqrt{2\nu} \frac{\|\mathbf{x}-\mathbf{x}'\|_2}{\lambda} \right), \quad (11)$$

where λ is the correlation length, which controls the spatial scale of correlations in the field, σ^2 is the marginal variance, representing the overall magnitude of field fluctuations, the smoothness parameter ν enables the generation of flow field solution ranging from highly irregular to moderately smooth, $\Gamma(\nu)$ is the gamma function, and K_ν is the modified second kind of Bessel function.

Diverse and broadband field data can be sampled from Matérn kernel parameters, and using fast Fourier transform (FFT),

$$u(\mathbf{x}) = \mu(\mathbf{x}) + \mathcal{F}^{-1} \left[\sqrt{\mathcal{F}[C(\mathbf{x}, \mathbf{x}')] \cdot \mathcal{F}[z(\mathbf{x})]} \right], \quad (12)$$

where $z(\mathbf{x}) \sim \mathcal{N}(0,1)$, \mathcal{F} and \mathcal{F}^{-1} represent the Fourier transform and its inverse transform, respectively. With a complexity of $\mathcal{O}(N \log N)$, this method is efficient for generating massive amount of flow field data, where N is the number of spatial points.

Specifically, for divergence-free velocity vector fields, scalar potentials ϕ_x , ϕ_y , and ϕ_z are first generated independently using Eq. (12), and then constructed by

$$\mathbf{u}(\mathbf{x}) = \left(\frac{\partial \phi_z}{\partial y} - \frac{\partial \phi_y}{\partial z}, \frac{\partial \phi_x}{\partial z} - \frac{\partial \phi_z}{\partial x}, \frac{\partial \phi_y}{\partial x} - \frac{\partial \phi_x}{\partial y} \right), \quad (13)$$

which is automatic satisfying $\nabla \cdot \mathbf{u}(\mathbf{x}) = 0$. For two-dimensional divergence-free velocity fields, the construction is simplified as $\mathbf{u}(\mathbf{x}) = \left(\frac{\partial \phi}{\partial y}, -\frac{\partial \phi}{\partial x} \right)$.

(2) Forward generation method of flow field solution with spectra constraint

An alternative generation method for flow field solutions is to make the solution follow spectrum constraint. Therefore, the samples naturally satisfy statistic properties in frequency domain. Saad and Sutherland [22] for generating divergence-free turbulent velocity fields based on turbulent kinetic spectrum $E(|\boldsymbol{\kappa}|)$,

$$\mathbf{u}(\mathbf{x}) = 2 \sum_{m=0}^M \sqrt{E(|\boldsymbol{\kappa}_m|) \Delta |\boldsymbol{\kappa}|} \cos(|\boldsymbol{\kappa}_m| \hat{\mathbf{r}}_m \cdot \mathbf{x} + \psi_m) \hat{\boldsymbol{\sigma}}_m, \quad (14)$$

where $|\boldsymbol{\kappa}| = \sqrt{\kappa_x^2 + \kappa_y^2 + \kappa_z^2}$ is the wave number, $\boldsymbol{\kappa}_m$ and ψ_m are the wave vector and phase of the m^{th} mode, $\boldsymbol{\kappa}_m = (|\boldsymbol{\kappa}_m| \sin(\theta_m) \cos(\varphi_m), |\boldsymbol{\kappa}_m| \sin(\theta_m) \sin(\varphi_m), |\boldsymbol{\kappa}_m| \cos(\theta_m))$, $\hat{\mathbf{r}}_m$ is the unit direction vector of $\boldsymbol{\kappa}_m$, $\hat{\boldsymbol{\sigma}}_m$ is a unit direction vector satisfying $\hat{\mathbf{r}}_m \cdot \hat{\boldsymbol{\sigma}}_m = 0$, M is the number of modes. We extend and derive a general formulation for generating scalar field (pressure, density, velocity components, etc.) based on any given spectrum $E_\phi(|\boldsymbol{\kappa}|)$,

$$u(\mathbf{x}) = 2 \sum_{m=0}^M \sqrt{\frac{1}{2} E_\phi(|\boldsymbol{\kappa}_m|) \Delta |\boldsymbol{\kappa}|} \cos(|\boldsymbol{\kappa}_m| \mathbf{x} + \psi_m), \quad (15)$$

Utilizing Eqs. (14)-(15), abundant vector and scale flow fields consistent with a given spectrum can be efficiently generated with a complexity of $\mathcal{O}(M \cdot N)$. In each mode, θ_m , φ_m and ψ_m are randomly

sampled from the uniform distribution within $[0, 2\pi]$ ($\mathcal{U}(0, 2\pi)$), ensuring randomness and diversity while maintaining statistical consistency with the target spectrum.

(3) Forward generation of data pairs satisfying partial differential equations

Using Eqs. (12)-(13) or Eqs. (14)-(15), flow field data with specific statistical or spectral properties can be efficiently generated. The initial velocity field can be generated using Eq. (13) or Eq. (14). The convective term $\mathbf{u} \cdot \nabla \mathbf{u}$ and the diffusive term $\nabla^2 \mathbf{u}$ are forward computed by substituting the generated velocity field \mathbf{u} into their formulations. These terms are further substituted into the governing PDEs to compute the remaining terms as source term to ensure the balance of governing equations. Thus the forward generated solution, initial conditions and remaining source term collectively form the training data pairs.

Specifically, for the pressure Poisson equation (Eq. (1b)) derived from the Navier-Stokes equations, the pressure field $p(\mathbf{x})$ is first generated using Eq. (12) or Eq. (15), and then forward construct the right-hand side of the equation (source term) by computing $\nabla^2 p(\mathbf{x})$, together with $p(\mathbf{x})$ forming the training data pairs.

Once the flow field data is generated, boundary conditions are assigned according to the specific problem. For a Dirichlet boundary condition with value u_b at boundary \mathbf{x}_b , set $u(\mathbf{x}_b) = u_b$. For a periodic boundary condition with period L_x , enforce $u(\mathbf{x} + L_x) = u(\mathbf{x})$, and for a Neumann boundary condition with boundary derivative $\left(\frac{\partial u}{\partial n}\right)_b$, apply $u\left(\mathbf{x}_b + \frac{1}{2}dx\right) = dx\left(\frac{\partial u}{\partial n}\right)_b + u\left(\mathbf{x}_b - \frac{1}{2}dx\right)$, where dx is the grid spacing at the boundary. To prevent numerical discontinuities (jumps) after boundary assignment, the smoothing filter is applied iteratively to smooth the field while preserving the boundary conditions. Therefore, this approach effectively combines flow field generation based on either GRF or spectra constraint with forward construction of boundary-constrained PDEs, ensuring the acquisition cost-efficiency and physical consistency of training data.

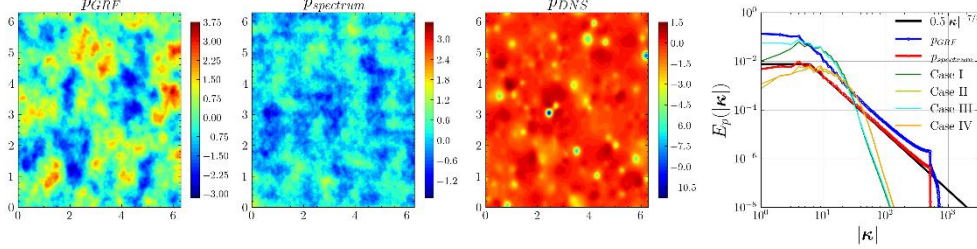
3. Results and discussion

3.1. Poisson-NN embedded solver for incompressible Navier-Stokes equations

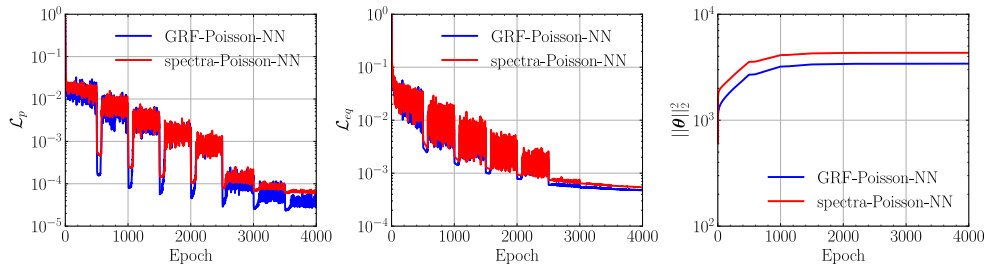
The 2D Kolmogorov flows [23] is first employed as the validation example. The Kolmogorov flow is defined on bi-periodic domain $[0, 2\pi L_{ref}] \times [0, 2\pi L_{ref}]$ with forcing $\mathbf{f} = \sin(\kappa y) \hat{\mathbf{x}}$, where κ is the spatial wavenumber and $\hat{\mathbf{x}} = (1, 0)$ is the unit vector in the x -direction. Simulations at $Re = 5,000$ are performed under initial conditions and forcing terms, listed in Table 1, where $\mathbf{u}_{0\text{GRF}} = \left(\frac{\partial \phi}{\partial y}, -\frac{\partial \phi}{\partial x}\right)$ is the divergence-free initial velocity field generated using Eq. (12) with Matérn kernel parameters $\lambda = 0.1$, $\nu = 1$, and $\sigma^2 = 1$ for the scalar potential ϕ , while $\mathbf{u}_{0\text{spectrum}}$ is generated using Eq. (14) with the von Kármán-Pao spectrum [24]. A finite difference scheme is performed on a staggered grid of size 1024×1024 , with the discrete coefficient matrix of PPE expressed as $\mathbf{A} = \mathbf{A}_x \otimes \mathbf{I}_y + \mathbf{I}_x \otimes \mathbf{A}_y$, where \mathbf{A}_x and \mathbf{A}_y are one-dimensional discrete matrices, \mathbf{I}_x and \mathbf{I}_y are identity matrices, \otimes denotes the Kronecker product.

Table 1. Some basic solution settings (dimensionless) for Kolmogorov flows

case	Re	dt	grid size	initial condition	source term \mathbf{f}
I	5,000	0.0005	1024×1024	$\mathbf{u}_{0\text{GRF}}$	$\sin(16y) \hat{\mathbf{x}}$
II					$\sin(32y) \hat{\mathbf{x}}$
III				$\mathbf{u}_{0\text{Spectrum}}$	$\sin(16y) \hat{\mathbf{x}}$
IV					$\sin(32y) \hat{\mathbf{x}}$

**Fig. 4.** Pressure fields and their spectra. From left to right: pressure using GRF ($\lambda = 0.1, \nu = 1, \sigma^2 = 1$) and spectral constrain, Case I at $t = 8$, and the corresponding pressure spectra (sample-averaged spectrum).

The high-fidelity dataset is critical for training a ML model. 400 pressure fields are generated separately using GRF- and spectral-constrain-based forward generation methods. For the GRF-based pressure fields (\mathbf{p}_{GRF}), the Matérn kernel parameters are sampled as follows: the correlation length $\lambda \sim \mathcal{U}(0.05, 0.1)$, the smoothness $\nu \sim \mathcal{U}(0.5, 3)$, and the marginal variance $\sigma^2 \sim \mathcal{U}(0.01, 3)$. For the spectral-constrain-based pressure fields ($\mathbf{p}_{\text{spectrum}}$), the pressure spectrum is given by $E_p(|\mathbf{k}|) = 0.5|\mathbf{k}|^{-7/3}$ [25], with the inertial range wavenumber lower limit set to 6, the spectrum value fixed below this threshold, and the upper mode limit set to $M = 512$. Subsequently, periodic boundary conditions are implemented by setting $p(\mathbf{x} = 2\pi) = p(\mathbf{x} = 0)$, and the corresponding right-hand side (source term) of the equation (\mathbf{b}_{GRF} and $\mathbf{b}_{\text{spectrum}}$) is constructed by $\mathbf{b} = \mathbf{A}\mathbf{p}$. Fig. 4 shows the generated (\mathbf{p}_{GRF} and $\mathbf{p}_{\text{spectrum}}$) and solved pressure fields (\mathbf{p}_{DNS}) along with their spectra. The spectrum of \mathbf{p}_{GRF} exhibits higher energy, indicating that the GRF-based method tends to overestimate the energy across scales, due to the wide range of sampled Matérn kernel parameters. The spectrum of $\mathbf{p}_{\text{spectrum}}$ aligns closely with the reference spectrum $E_p(|\mathbf{k}|) = 0.5|\mathbf{k}|^{-7/3}$, indicating that the spectral-constrained method effectively captures the target energy distribution within the inertial range.

**Fig. 5.** Training loss curves of the GRF-Poisson-NN and the spectra-Poisson-NN.

Poisson-NNs are trained on GRF-based and spectral-constrain-based datasets, with the training loss curves shown in Fig. 5. The learning rate starts at 1×10^{-3} and is halved every 500 epochs. The first 2,500 epochs use single precision, followed by double precision for the rest of the training. Fig. 6 compares the time-varying relative errors of the Poisson-NNs. Throughout the entire solution process, the relative error of $\mathbf{p}_{\text{NN}}(t)$ ($\epsilon_{\mathbf{p}_{\text{NN}}}(t) = \frac{\|\mathbf{p}_{\text{NN}}(t) - \mathbf{p}_{\text{DNS}}(t)\|_2}{\|\mathbf{p}_{\text{DNS}}(t)\|_2}$) consistently remains smaller than the relative

error between consecutive time steps ($\frac{\|\mathbf{p}_{DNS}(t-dt)-\mathbf{p}_{DNS}(t)\|_2}{\|\mathbf{p}_{DNS}(t)\|_2}$). For cases I-IV, the time-averaged relative errors between two consecutive time steps are 2.10×10^{-3} , 2.40×10^{-3} , 2.14×10^{-3} , and 2.38×10^{-3} , respectively, while the time-averaged relative errors of $\mathbf{p}_{NN}(t)$ ($\bar{\epsilon}_{\mathbf{p}_{NN}}$) decreased to 2.03×10^{-4} , 8.48×10^{-4} , 2.25×10^{-4} , and 8.83×10^{-4} for the GRF-based network, further reduced to 2.91×10^{-5} , 1.01×10^{-4} , 2.77×10^{-5} , and 1.02×10^{-4} for spectra-based network. Since $\mathbf{p}_{NN}(t)$ does not yet meet the high precision requirement of 1×10^{-6} , it serves as the initial approximation very close to exact solution for the regular MG solver (with Jacobi smoother and linear interpolation for restriction and prolongation operations), which can significantly reduce the number of iterations required and remarkably accelerate the overall solution process.

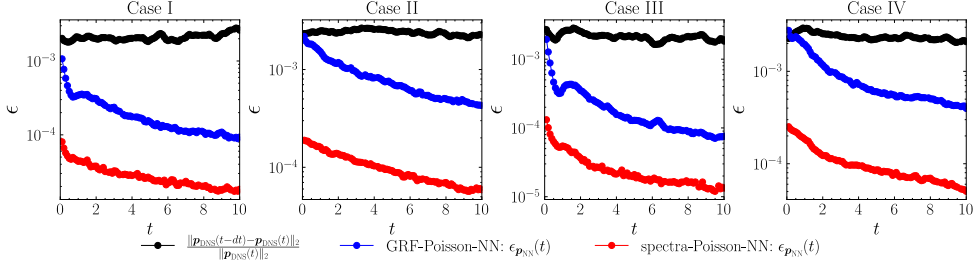


Fig. 6. Comparison of time-varying relative errors in the Kolmogorov flow tasks, black lines show the relative error between consecutive time steps, $\frac{\|\mathbf{p}_{DNS}(t-dt)-\mathbf{p}_{DNS}(t)\|_2}{\|\mathbf{p}_{DNS}(t)\|_2}$, while blue and red lines represent the relative errors of GRF-Poisson-NN and spectra-Poisson-NN, respectively, $\epsilon_{\mathbf{p}_{NN}}(t) = \frac{\|\mathbf{p}_{NN}(t)-\mathbf{p}_{DNS}(t)\|_2}{\|\mathbf{p}_{DNS}(t)\|_2}$.

The spectra of \mathbf{p}_{DNS} and the spectra of \mathbf{p}_{NN} for GRF-Poisson-NN and spectra-Poisson-NN are further compared in Fig. 7. Both GRF-Poisson-NN and spectra-Poisson-NN accurately approximate the pressure spectra in the low wavenumber range. The approximated pressure spectra for GRF-Poisson-NN gradually deviates below the spectra of \mathbf{p}_{DNS} at wavenumbers $|\kappa| > 10^2$, whereas spectra-Poisson-NN maintains a closer approximation until $|\kappa| > 3 \times 10^2$. Therefore, spectra-Poisson-NN achieves a better high-frequency approximation compared to GRF-Poisson-NN.

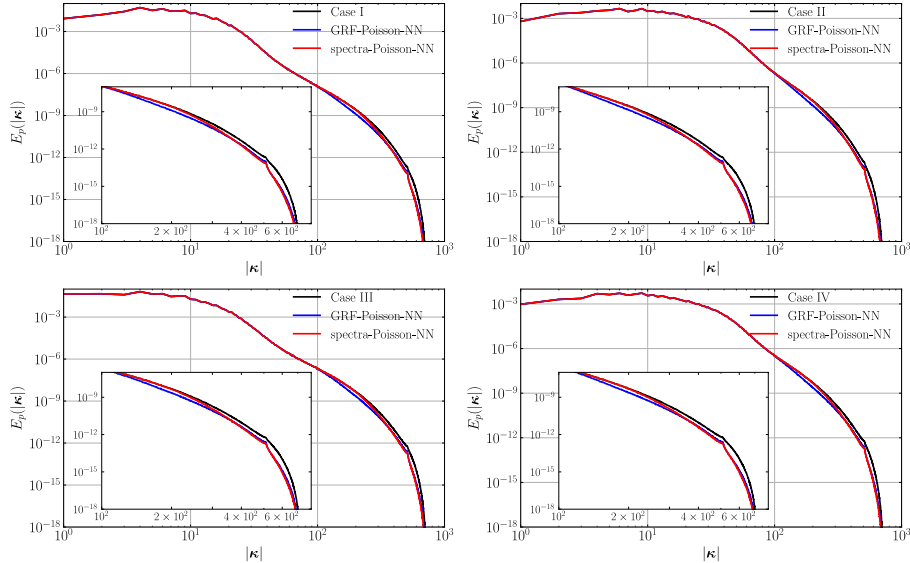


Fig. 7. Comparison of pressure spectra in the Kolmogorov flow tasks, black lines represent the spectra of \mathbf{p}_{DNS} (the time-averaged spectrum), while blue and red lines correspond to the spectra of \mathbf{p}_{NN} for GRF-Poisson-NN and spectra-Poisson-NN, respectively.

The comparison of iteration counts is shown in Fig. 8. The average solution speed of the GRF-Poisson-NN embedded solver for cases I-IV is 5.53, 3.68, 6.06, and 3.73 times that of MG (with $\mathbf{p}_{\text{DNS}}(t - dt)$ as the initial guess), the spectra-Poisson-NN embedded solver is 5.78, 3.96, 6.41, and 4.01 times that of MG. Experimental results show that spectra-Poisson-NN outperforms GRF-Poisson-NN. As seen in Fig. 5, GRF-Poisson-NN fits the GRF-based dataset more easily, while Fig. 4 reveals excessive spectral energy in the inertial range for GRF-based pressure fields. In contrast, spectra-Poisson-NN, with more physically consistent training data, provides better generalization and consistency.

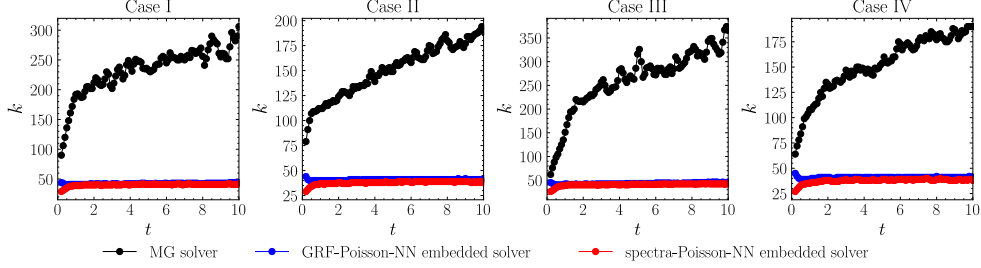


Fig. 8. Comparison of iteration counts in the Kolmogorov flow tasks, black lines show the iteration counts of MG with $\mathbf{p}_{\text{DNS}}(t - dt)$ as the initial guess, while blue and red lines represent the iteration counts of GRF-Poisson-NN embedded solver and spectra-Poisson-NN embedded solver, respectively.

The Poisson-NN embedded solver is subsequently applied to simulate decaying flow. Decaying flow begins with the velocity field of a fully developed Kolmogorov flow as the initial condition, allowing it to evolve freely without external forcing ($\mathbf{f} = \mathbf{0}$). Over time, small-scale vortices gradually merge into larger vortices, resulting in changes to the Reynolds number. The decaying flows listed in Table 2 are simulated to evaluate the speed-up performance of the Poisson-NN embedded solver. The spatial discretization scheme used for these simulations remains consistent with that employed for the Kolmogorov flows.

Table 2. Some basic solution settings for decaying flows

case	initial Re	kinematic viscosity	dt	grid size	initial condition
V	5,000	2×10^{-4}	0.0005	1024×1024	$\mathbf{u}(t = 10)$ from Case I
VI					$\mathbf{u}(t = 10)$ from Case II
VII					$\mathbf{u}(t = 10)$ from Case III
VIII					$\mathbf{u}(t = 10)$ from Case IV

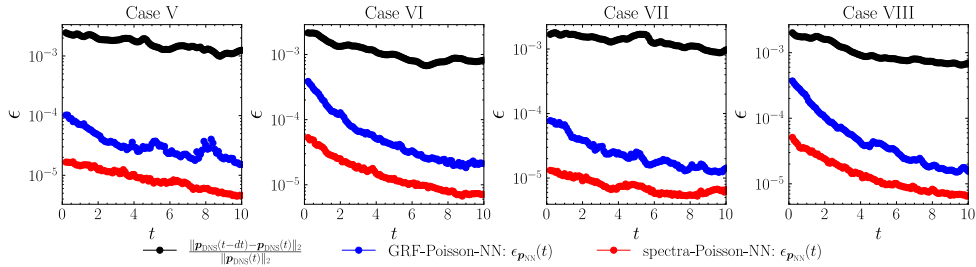


Fig. 9. Comparison of time-varying relative errors in the decaying flow tasks.

The Poisson-NNs do not require retraining and directly use the previously well-trained models in the solution process. Similarly, the time-varying relative errors of the Poisson-NNs are compared, as shown in Fig. 9. The relative error curves of \mathbf{p}_{NN} consistently remain below than the relative error between two consecutive time steps, and the spectra-Poisson-NN outperforms the GRF-Poisson-NN. The time-

averaged relative errors between two consecutive time steps for cases V-VIII are 1.63×10^{-3} , 1.10×10^{-3} , 1.35×10^{-3} , and 1.04×10^{-3} , respectively, while $\bar{\epsilon}_{p_{NN}}$ decreased to 3.56×10^{-5} , 7.30×10^{-5} , 2.70×10^{-5} , and 6.90×10^{-5} for the GRF-based network, reducing by nearly 1.5 orders of magnitude, further reduced to 9.21×10^{-6} , 1.65×10^{-5} , 7.62×10^{-6} , and 1.54×10^{-5} for spectra-based network, reducing by nearly two orders of magnitude. The spectra of p_{DNS} and the spectra of p_{NN} for GRF-Poisson-NN and spectra-Poisson-NN shown in Fig. 10 further demonstrate that the high-frequency approximation performance of spectra-Poisson-NN is superior to that of GRF-Poisson-NN. The comparison of iteration counts in the decaying flow tasks is shown in Fig. 11. The GRF-Poisson-NN embedded solver achieves average solution speeds of 5.74, 4.25, 5.87, and 4.88 times faster than MG for cases V-VIII, respectively, while the spectra-Poisson-NN embedded solver achieves speeds of 7.49, 5.65, 7.69, and 5.64 times faster, demonstrating a significant improvement.

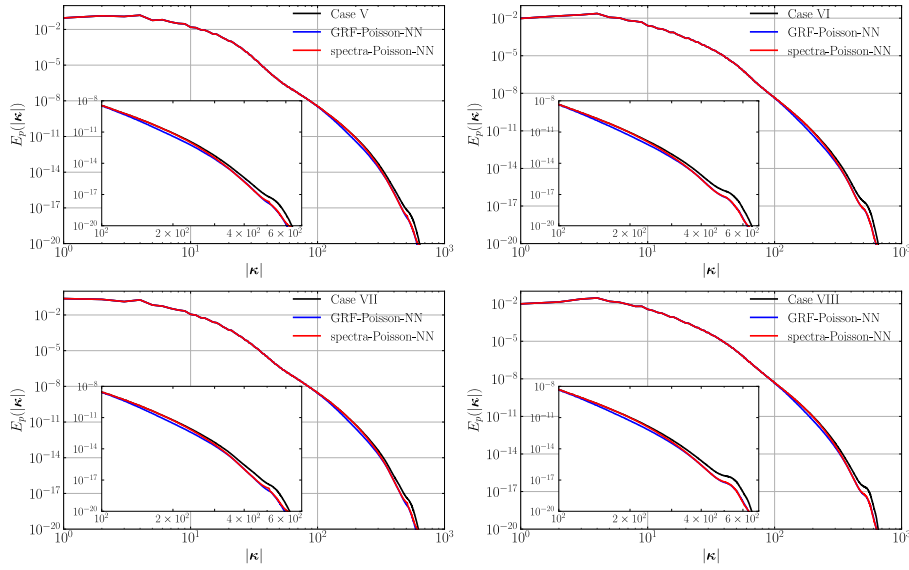


Fig. 10. Comparison of pressure spectra in the decaying flow tasks.

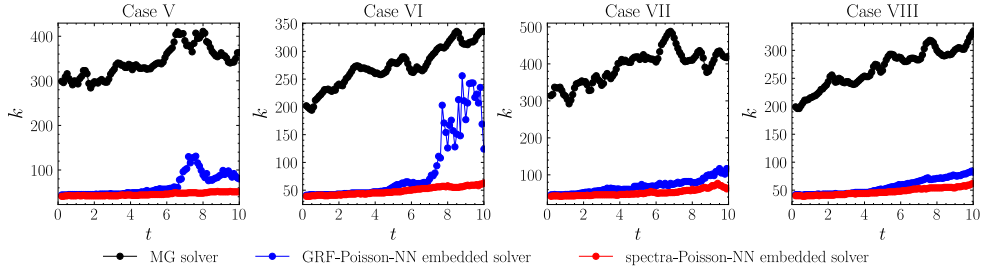


Fig. 11. Comparison of iteration counts in the decaying flow tasks.

3.2. Wavelet transform CNN multigrid for PPE

Using the spectral-constrain-based dataset from Section 3.1 to train WTCNN-MG for solving the PPE of the Kolmogorov flows list in Table 1 and the decaying flows list in Table 2. For comparison, MG, neural multigrid (NMG), and CNN embedded multigrid (CNN-MG) with hierarchical structures consistent with WTCNN-MG are also constructed. MG is the classical MG with Jacobi smoother and linear interpolation for restriction and prolongation operations. NMG is derived from WTCNN-MG by removing WTCNN. CNN-MG substitutes WTCNN with CNN and replaces DWT and IDWT with

convolution and transposed convolution operations (stride $s = 2$), maintaining the same hidden layer channels as WTCNN-MG.

The training process involves up to 20 V-cycles and 800 optimization epochs per model. A variable learning rate starts at 1×10^{-3} , halving every 100 epochs. The first 500 iterations are trained using single precision, and the last 300 iterations switch to double precision. Fig. 12 shows the training loss curves of NMG, CNN-MG and WTCNN-MG in the 20th V-cycle, where WTCNN-MG achieves a final loss nearly one order of magnitude lower than NMG and CNN-MG. The sharp loss reduction upon switching to double precision highlights its necessity, especially as single precision approaches its limits, providing significant improvements for WTCNN-MG.

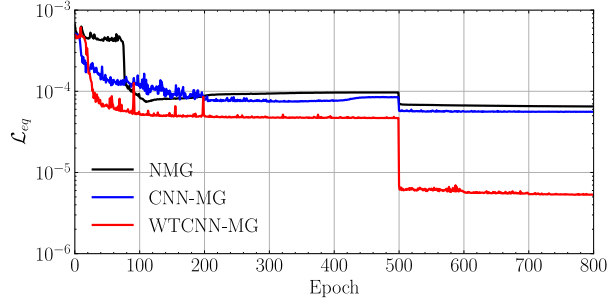


Fig. 12. Training loss curves of NMG, CNN-MG and WTCNN-MG in the 20th V-cycle.

The performance is compared in terms of convergence, iteration counts, and speedup factor, with partial results in the Kolmogorov flow tasks shown in Fig. 13, indicating that WTCNN-MG outperforms all other models. WTCNN-MG reduced the relative residual by two orders of magnitude compared to MG and one order compared to NMG and CNN-MG after just one iteration, requiring significantly fewer iterations to achieve the same residual level. When the relative residuals reduce to 1×10^{-6} , WTCNN-MG achieves average speedups of 6.59, 11.55, 7.00, and 11.00 times over MG for cases I-IV, outperforming the Poisson-NN embedded solver with greater acceleration. Additionally, WTCNN-MG is 5.45, 7.39, 5.35, and 7.13 times faster than NMG and 3.99, 5.39, 4.18, and 5.38 times faster than CNN-MG for the same cases.

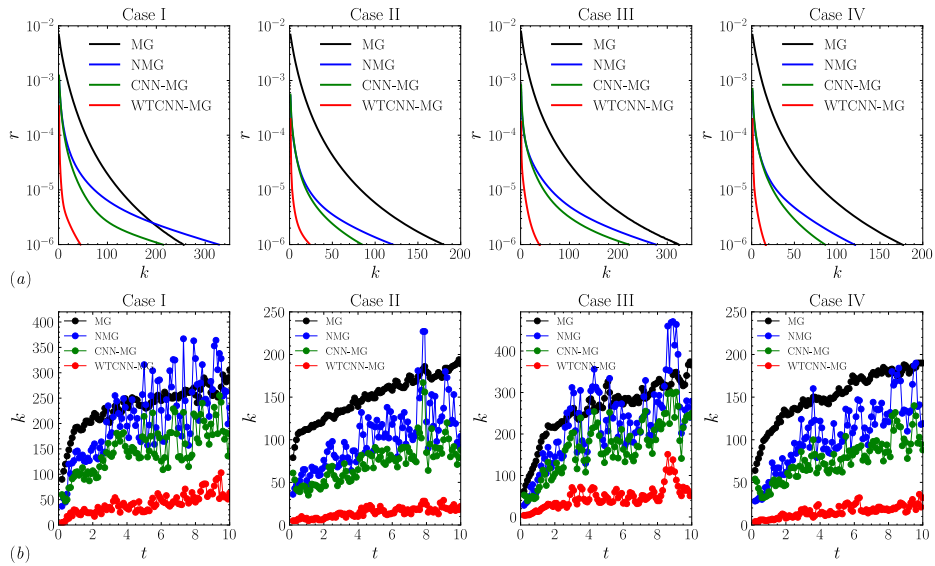


Fig. 13. Partial comparison results of MG, NMG, CNN-MG and WTCNN-MG in the Kolmogorov flow tasks, (a) iteration convergence process for Cases I-IV at $t = 8$, (b) iteration counts for Cases I-IV when $r = \frac{\|Ap-b\|_2}{\|b\|_2} < 10^{-6}$. The iteration count k represents the number of V-cycles.

The comparison results of these models in the decaying flow tasks are shown in Fig. 14. WTCNN-MG demonstrated the best convergence performance across all cases, with a convergence rate significantly surpassing other models. Notably, for case VI and case VIII, after the decaying flow evolves to $t > 4$, the relative residual of CNN-MG eventually stagnates at 2×10^{-6} . Under conditions of convergence, the number of iterations of CNN-MG are fewer than that of MG and NMG, which indicates that the CNN in CNN-MG corrects the smoothing error to a certain extent. In contrast, WTCNN combines the advantages of wavelet transform-based multilevel analysis and CNN feature extraction, more effectively correcting low-frequency smoothing errors while demonstrating superior robustness and generalization. When the relative residuals reduce to 1×10^{-6} , WTCNN-MG is 4.69, 5.49, 4.26, and 5.65 times faster than MG for cases V-VIII, and 4.28, 3.96, 3.92, and 4.53 times faster than NMG, highlighting its efficiency.

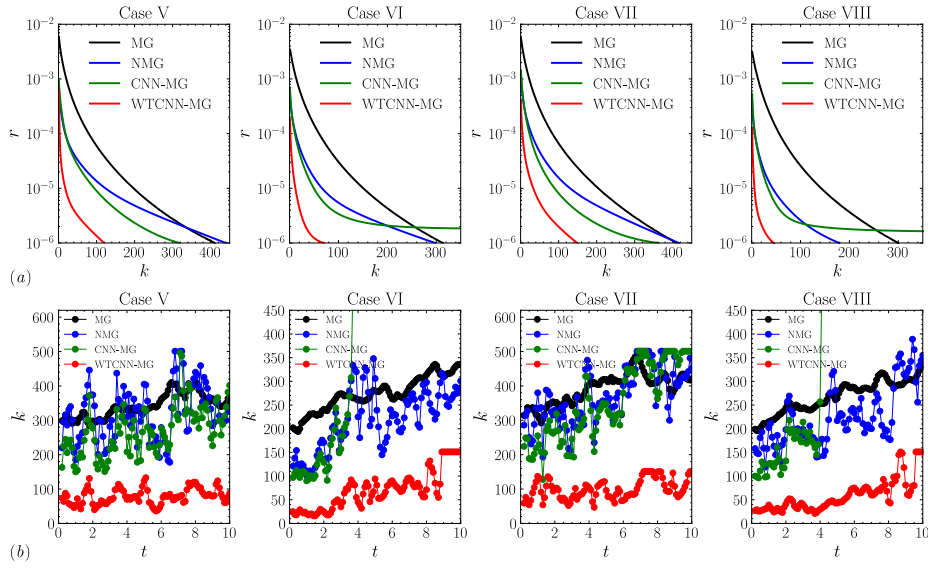


Fig. 14. Partial comparison results of MG, NMG, CNN-MG and WTCNN-MG in the decaying flow tasks, (a) iteration convergence process for Cases I-IV at $t = 8$, (b) iteration counts for Cases I-IV when $r = \frac{\|Ap-b\|_2}{\|b\|_2} < 10^{-6}$. The iteration count k represents the number of V-cycles.

Table 3. Some basic solution settings for PPE of 3D isotropic flows

case	solution domain	grid size	boundary condition	pressure spectrum
IX	$[0, 2\pi] \times [0, 2\pi] \times [0, 2\pi]$	$256 \times 256 \times 256$	tri-directional periodic	$E_p(\kappa) = 0.5 \kappa ^{-7/3}$
X				$E_p(\kappa) = 1.0 \kappa ^{-7/3}$
XI				$E_p(\kappa) = 5.0 \kappa ^{-7/3}$
XII				$E_p(\kappa) = 10.0 \kappa ^{-7/3}$

The concept of generating training datasets using spectra constraint is further applied to train WTCNN-MG for solving the PPE of three dimensional (3D) isotropic flows list in Table 3. Similarly, 50 spectral-constrain-based pressure fields are generated using Eq. (15) and the reference spectrum $E_p(|\kappa|) = 0.5|\kappa|^{-7/3}$, with the upper mode limit set to $M = 128$. The tri-directional periodic boundary conditions are implemented by setting $p(\mathbf{x} = 2\pi) = p(\mathbf{x} = 0)$, and then the right-hand side of the PPE is constructed by $\mathbf{b} = A\mathbf{p}$ as the training dataset.

Fig. 15 compares the iterative convergence process of MG, NMG, CNN-MG, and WTCNN-MG for the PPE of 3D isotropic flows. The convergence rate follows the sequence of WTCNN-MG, NMG, and MG, indicating that WTCNN-MG not only enhances spectral properties by optimizing smoothing, differentiation, restriction, and prolongation, but also effectively correcting low-frequency smoothing errors through WTCNN. CNN-MG stagnates at relative residuals of 2×10^{-5} and 8×10^{-6} in cases IX and XI, and diverges in cases X and XII (which deviate significantly from the training data spectrum), revealing severe overfitting and poor generalization. In contrast, WTCNN-MG consistently converges to 1×10^{-6} across all cases, demonstrating superior robustness and generalization. WTCNN-MG is 10.33, 7.44, 5.51, and 4.13 times faster than MG and 2.50, 3.69, 3.93, and 3.25 times faster than NMG for residual thresholds of 1×10^{-3} , 1×10^{-4} , 1×10^{-5} , and 1×10^{-6} , respectively.

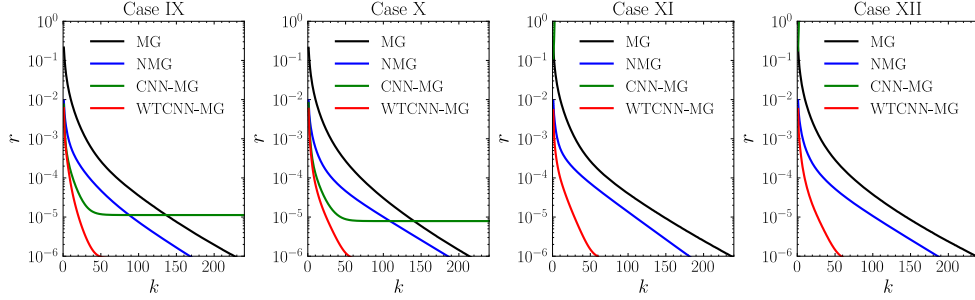


Fig. 15. The iterative convergence process of MG, NMG, CNN-MG, and WTCNN-MG for the PPE of 3D isotropic flows.

4. Conclusions

This study proposes a high-efficient ML projection method using forward-generated data for incompressible Navier-Stokes equations. A Poisson neural network (Poisson-NN) embedded method and a wavelet transform convolutional neural network multigrid (WTCNN-MG) method are proposed, integrated into the projection method framework in patchwork and overall differentiable manners with the MG method, respectively. Forward generation methods of flow field solution with GRF and spectra constraint are presented, the former with a computational complexity of $\mathcal{O}(N \log N)$, providing statistical consistency, and the latter with a computational complexity of $\mathcal{O}(N \cdot M)$, ensuring spectral consistency. The data pairs of source terms, boundary conditions and initial conditions with corresponding solutions of governing PDEs is constructed via balance of PDEs, avoiding the difficulties of obtaining high-fidelity training datasets that are expensive or even inaccessible. The feasibility of generated data for training Poisson-NN and WTCNN as well as the acceleration performances of the Poisson-NN embedded method and WTCNN-MG method are validated. The results indicate that even without any DNS data, the generated data can train these two models with excellent generalization and accuracy. The data following spectrum can significantly improve the high-frequency approximation, convergence rate, generalization and accuracy than that generated following GRF. The ML projection method offers significant improvements in computational efficiency. Particularly, the Poisson-NN embedded method achieves an average 5.83 times speed-up compared to the traditional MG method, while the WTCNN-MG method performs better, with an average 7.03 times speed-up. The ML projection method and data forward

generation method have broad application potential, and further studies on anisotropic turbulent flow with separating, attaching, transition, and etc. will be performed in the future.

Acknowledgements

This research was funded by the National Natural Science Foundation of China (Grant Nos. 51921006, 92152301, 52108452).

Declaration of interests

The authors report no conflict of interest.

References

- [1] S.L. Brunton, B.R. Noack, P. Koumoutsakos, Machine learning for fluid mechanics, *Annual review of fluid mechanics*, 52 (2020) 477-508.
- [2] R. Vinuesa, S.L. Brunton, Enhancing computational fluid dynamics with machine learning, *Nature Computational Science*, 2 (2022) 358-366.
- [3] C. Chen, H. Li, X. Jin, An invariance constrained deep learning network for partial differential equation discovery, *Physics of Fluids*, 36 (2024).
- [4] C. Jiang, R. Vinuesa, R. Chen, J. Mi, S. Laima, H. Li, An interpretable framework of data-driven turbulence modeling using deep neural networks, *Physics of Fluids*, 33 (2021).
- [5] Y. Bar-Sinai, S. Hoyer, J. Hickey, M.P. Brenner, Learning data-driven discretizations for partial differential equations, *Proceedings of the National Academy of Sciences*, 116 (2019) 15344-15349.
- [6] D. Kochkov, J.A. Smith, A. Alieva, Q. Wang, M.P. Brenner, S. Hoyer, Machine learning-accelerated computational fluid dynamics, *Proceedings of the National Academy of Sciences*, 118 (2021) e2101784118.
- [7] E. Ajuria Illarramendi, A. Alguacil, M. Bauerheim, A. Misdariis, B. Cuenot, E. Benazera, Towards an hybrid computational strategy based on deep learning for incompressible flows, in: *AIAA Aviation 2020 Forum*, 2020, pp. 3058.
- [8] E.A. Illarramendi, M. Bauerheim, B. Cuenot, Performance and accuracy assessments of an incompressible fluid solver coupled with a deep convolutional neural network, *Data-Centric Engineering*, 3 (2022) e2.
- [9] R. Chen, X. Jin, H. Li, A machine learning based solver for pressure Poisson equations, *Theoretical and Applied Mechanics Letters*, 12 (2022) 100362.
- [10] Y. Li, P.Y. Chen, T. Du, W. Matusik, Learning preconditioners for conjugate gradient PDE solvers, in: *International Conference on Machine Learning*, PMLR, 2023, pp. 19425-19439.
- [11] A. Katrutsa, T. Daulbaev, I. Oseledets, Deep multigrid: learning prolongation and restriction matrices, *arXiv preprint arXiv:1711.03825*, (2017).
- [12] A. Katrutsa, T. Daulbaev, I. Oseledets, Black-box learning of multigrid parameters, *Journal of Computational and Applied Mathematics*, 368 (2020) 112524.
- [13] D. Greenfeld, M. Galun, R. Basri, I. Yavneh, R. Kimmel, Learning to optimize multigrid PDE solvers, in: *International Conference on Machine Learning*, PMLR, 2019, pp. 2415-2423.
- [14] I. Luz, M. Galun, H. Maron, R. Basri, I. Yavneh, Learning algebraic multigrid using graph neural networks, in: *International Conference on Machine Learning*, PMLR, 2020, pp. 6489-6499.
- [15] A. Taghibakhshi, S. MacLachlan, L. Olson, M. West, Optimization-based algebraic multigrid coarsening using reinforcement learning, *Advances in neural information processing systems*, 34 (2021) 12129-12140.
- [16] J. He, J. Xu, MgNet: A unified framework of multigrid and convolutional neural network, *Science china mathematics*, 62 (2019) 1331-1354.
- [17] Y. Chen, B. Dong, J. Xu, Meta-mgnet: Meta multigrid networks for solving parameterized partial differential equations, *Journal of computational physics*, 455 (2022) 110996.
- [18] V. Fanaskov, Neural multigrid architectures, in: *2021 International Joint Conference on Neural Networks (IJCNN)*, IEEE, 2021, pp. 1-8.
- [19] A.J. Chorin, Numerical solution of the Navier-Stokes equations, *Mathematics of computation*, 22 (1968) 745-762.
- [20] Y. Saad, *Iterative methods for sparse linear systems*, SIAM, 2003.
- [21] Z.-Q.J. Xu, Y. Zhang, T. Luo, Y. Xiao, Z. Ma, Frequency principle: Fourier analysis sheds light on deep neural networks, *arXiv preprint arXiv:1901.06523*, (2019).

- [22] T. Saad, J.C. Sutherland, Comment on “Diffusion by a random velocity field”[Phys. Fluids 13, 22 (1970)], Physics of Fluids, 28 (2016).
- [23] G.J. Chandler, R.R. Kerswell, Invariant recurrent solutions embedded in a turbulent two-dimensional Kolmogorov flow, Journal of Fluid Mechanics, 722 (2013) 554-595.
- [24] C. Bailly, D. Juve, A stochastic approach to compute subsonic noise using linearized Euler's equations, in: 5th AIAA/CEAS aeroacoustics conference and exhibit, 1999, pp. 1872.
- [25] T. Gotoh, D. Fukayama, Pressure spectrum in homogeneous turbulence, Physical Review Letters, 86 (2001) 3775.